Intracranial recordings reveal ubiquitous in-phase and in-antiphase functional connectivity between homologous brain regions in humans

Christian O'Reilly*[a] and Mayada Elsabbagh[a]

[a] Montreal Neurological Institute-Hospital, Azrieli Centre for Autism Research, McGill University, Montreal, Canada

Corresponding author:

Christian O'Reilly, Ph.D.

3775 Rue University, Room C18

Duff Medical Building

Montréal, Québec, H3A 2B4

christian.oreilly@mcgill.ca

1-438-933-3696

Abstract

Whether neuronal populations exhibit zero-lag (in-phase or in-antiphase) functional connectivity is a fundamental question when conceptualizing communication between cell assemblies. It also has profound implications on how we assess such interactions. Given that the brain is a delayed network due to the finite conduction velocity of the electrical impulses traveling across its fibers, the existence of zero-lag functional connectivity may be considered improbable. However, in this study, using intracranial recordings we demonstrate that most inter-hemispheric connectivity between homologous cerebral regions is zero-lagged and that this type of connectivity is ubiquitous. Volume conduction can be safely discarded as a confounding factor since it is known to drop almost completely within short inter-electrode distances (< 20 mm) in intracranial recordings. This finding should guide future electrophysiological connectivity studies and highlight the importance of considering the role of zero-lag connectivity in our understanding of communication between cell assemblies.

Introduction

The human brain is among the most complex networks known to humanity. It is estimated to comprise about 86 billion neurons (Azevedo et al., 2009), supported by as many glial cells (Azevedo et al., 2009; von Bartheld et al., 2016) and a sophisticated vasculature mesh. In the neocortex alone, neurons are interconnected by around 0.15 quadrillion synapses (Pakkenberg et al., 2003). Interactions within this vast network are enabled by mechanisms operating at distinct spatial and temporal scales. For example, while subcellular exchanges such as synaptic firing occur within milliseconds, other mechanisms like plasticity may involve days-long neural reorganization across broad cortical regions (Bassett and Sporns, 2017; Betzel and Bassett, 2017). Our understanding of these phenomena depends on our ability to measure brain activity across a spectrum of spatio-temporal scales.

The electroencephalography (EEG) provides a time-resolved macroscopic correlate of cerebral activity. It can be recorded when synchronous discharges of spatially aligned populations of neurons, like the pyramidal cells, generate a cumulative electrical field that propagates by *volume conduction* from its source all the way to the scalp, where it can be picked up using surface electrodes. Unfortunately, the same volume conduction that makes EEG possible has been shown to be a major confounder for functional connectivity based on EEG (Nunez et al., 1997).

Unfolding this paradoxical role of volume conduction requires taking a closer look at the concept of EEG functional connectivity. Electrophysiological connectivity is generally considered a correlate of functional interaction due to saltatory conduction (i.e., the transmission of information through action potentials) propagated to single electrodes by short-range volume conduction. Ideally, there would be no long-range volume-conducted potentials reaching more

than one electrode and no parallel means of communication, such as ephaptic coupling (Anastassiou et al., 2011) (i.e., modulation of neuronal computation by volume-conducted electrical fields). However, this ideal hangs on a very delicate trade-off between two opposite requirements; the neuronal activity must encompass a cell population sufficiently large to produce a measurable voltage deflection, while at the same time be sufficiently spatially-retrained as to not overlap with regions covered by the other electrodes.

Moreover, the concept of functional connectivity, and the way it is reflected in EEG signals, shifts gradually across spatial scales. At a small scale, local connectivity is reflected directly in EEG amplitude since it depends on the synchronous activation of large neuronal populations. As we move to a larger scale, the connectivity can no longer be measured on a single EEG lead, but it rather relies on statistical dependence (e.g., coherence) between pairs of EEG signals generated by overlapping mixtures of neuronal sources. This overlap diminishes gradually as the scale — or equivalently the inter-electrode distance — becomes larger up to the point where volume conduction fully dissipates. In EEG, this distance is relatively large; for example, coherence measures have been determined to be significantly impacted by volume conduction for pairs of electrodes separated by at least up to 100 mm (Srinivasan et al., 1998). For smaller distances, an undetermined proportion of the statistical dependence is due to volume conduction from common neuronal sources rather than connectivity.

To overcome this severe limitation, neuronal communication based on action potentials needs to be distinguished from spurious dependencies due to volume conduction. Using the quasistatic approximation of Maxwell's equations, volume conduction has been shown to propagate instantaneously for EEG (Plonsey and Heppner, 1967) and is therefore known to be a sufficient, but not a necessary, condition for in-phase EEG activity between distant locations

on the scalp. Such in-phase synchronization has consequently often been downplayed as an artifact of volume conduction. For example, studies relying only on the *imaginary part of coherency* (Nolte et al., 2004) or the *phase lag index* (Stam et al., 2007), discard *by-design* any non-lagged activity between pairs of channels, regardless of whether it is an artifact or the result of genuine functional connectivity synchronized with no lag. This contrasts sharply with fundamental (Varela et al., 2001), experimental (Campo et al., 2019; Gray et al., 1989; Roelfsema et al., 1997), and modeling studies (Dalla Porta et al., 2019; Vicente et al., 2008; Viriyopase et al., 2012) supporting the existence of zero-lag neuronal connectivity.

Therefore, despite being treated as an artifact of volume conduction, zero-lag connectivity may be an important yet neglected mechanism underlying neural network communication. To investigate this possibility, we turned to intracranial recording (Frauscher et al., 2018), which is sensitive to volume-conducted activity from much smaller regions (< 20 mm; (T. H. Bullock et al., 1995; T H Bullock et al., 1995; Nunez et al., 1997)) than EEG (< 100 mm; (Srinivasan et al., 1998)) due to the greater proximity between electrodes and neuronal sources. By introducing a one-sample offset between intracranial signals, we evaluated the proportion of zero-lag connectivity that is discarded from the standard PLI measure in electrodes distant enough (> 35 mm) not to share common volume-conducted sources. In doing so, we uncover reliable and ubiquitous zero-lag connectivity – both in-phase and in-antiphase – between homologous cortical regions.

Results

Homologous brain regions exhibit ubiquitous zero-lag connectivity

We measured functional connectivity in intracranial recordings from 106 patients (54 males; mean age of 33.1 +/- 10.8 years) undergoing pre-surgical testing for drug-resistant

epilepsy(Frauscher et al., 2018); see methods for details). Namely, we computed PLI between every pair of electrodes in every subject, with and without an offset between the signals (offset-PLI and standard PLI, respectively).

Since PLI is known to be biased (i.e., it is systematically larger than zero even in absence of true connectivity), we computed a baseline corresponding to the chance level using a "surrogate" dataset. This surrogate dataset was obtained by randomly selecting a subset of 200 channels and computing PLI for every pair not belonging to the same patient (surrogate-PLI). As shown in Figure 1.a, there is a bias of approximately 0.1 for PLI computed on 1-second epochs irrespective of the frequency. Thus, we debaised any further PLI estimates by subtracting mean surrogate-PLI value (mean ± sd: 0.102 ± 0.013; N=78,303).

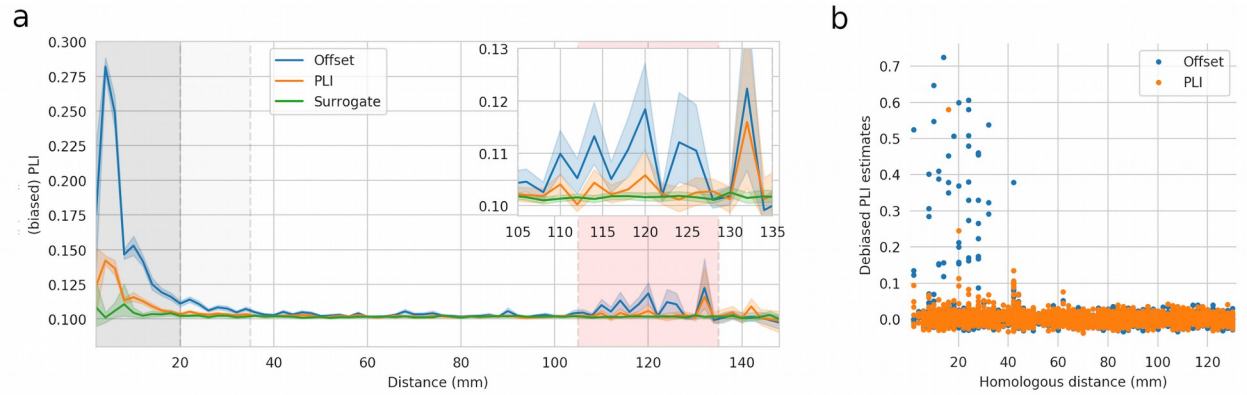

Figure 1. Standard and offset-PLI connectivity between pairs of channels. a) PLI values with respect to inter-electrode distances for the standard PLI definition (PLI; orange), the one-sample offset-PLI (offset; blue), and the PLI computed on surrogate data (surrogate; green). Shaded regions around the lines indicate the 95% confidence interval, computed using bootstrapping. The dark gray region delimits the range of distances for which we expect the presence of volume conduction. The pale gray region delineates a "safety margin" in which we do not interpret the connectivity results because of the possibility

that some effect of volume conduction remains. The pink region delimits a range of distances for which significant connectivity is observed and for which we are confident that there cannot be any volume conduction artifact for intracranial recordings. We refer to the distances within this range as *target distances* since they are the focus of our subsequent analyses. The inset shows a close view of the PLI for the target distances. b) Offset (blue) and standard PLI (orange) for pairs of electrodes within the target distance range plotted against their homologous distance (see text for the definition).

Zero-lag connectivity for results within the dark grey region (inter-electrode distance < 20 mm) of Figure 1.a are likely heavily inflated by volume conduction. The offset-PLI is still significantly different from the surrogate-PLI estimates up to around 35 mm. Although at such distances volume conduction should not have a major effect, any difference between surrogate-PLI and offset-PLI values is debatable. In contrast, we observe offset-PLI significantly above surrogate-PLI values within an approximate range of 105 to 135 mm (shown as a pink area in Figure 1.a), which is clearly far beyond the reach of volume conduction in intracranial recordings. As opposed to offset-PLI, estimated standard PLI are barely larger than surrogate-PLI within this target range with confidence intervals generally overlapping with surrogate-PLI estimates (see inset in Figure 1.a), clearly demonstrating that most of the significant long-range connectivity is happening without any lag.

Having demonstrated significant zero-lag long-range connectivity, we further investigated the possibility that it may reflect interhemispheric connections between homologous regions. We focused on within-subject electrode pairs separated by distances that fall within the 105 and 135 mm range. For these pairs, we computed their *homologous distance*, defined as the distance between two channels if the left hemisphere was mirrored over the right hemisphere. In

practice, since the mediolateral axis is centered on the interhemispheric fissure, this distance is obtained by using the absolute value of the channel coordinates along this axis.

Figure 1.b shows the relationship between the homologous distance and the standard PLI (orange) and offset-PLI (blue) values. It distinctly shows that all strong long-distance connections are established between channels with very short homologous distances. Further, all 46 channel pairs separated by distances falling within our target range and showing a debiased offset-PLI greater than 0.1 were from homologous regions. By contrast, such *homologous pairs* (i.e., channel pairs from homologous regions) constitute only 7.6% (N=228/2992) of the pairs with offset-PLI values smaller than 0.1. Among all homologous pairs, 16.8% (N=46/274) were showing debiased offset-PLI values of more than 0.1, whereas this ratio is 0% (N=0/2764) for non-homologous pairs. For the same electrode pairs, only six showed standard debiased PLI above 0.1, confirming our previous conclusion that most of the interhemispheric connectivity is happening at zero-lag. All of these six pairs were between homologous regions.

Highly connected pairs were observed in seven out of nine patients implanted with electrodes in homologous regions (see Table 1). The two remaining subjects had very few homologous pairs (3 and 4 pairs respectively). This large proportion of homologous pairs highly connected with zero-lag is surprising considering that they were obtained from only 60-second-long recordings of spontaneous activity, per subject and vigilance state.

Table 1. Number of homologous pairs per subject, number of these pairs that have an offset-PLI > 0.1, and their relative proportion in percentage.

Subject	Homologous pairs	Offset-PLI > .1	Proportion (%)
29	30	9	30.0%
40	9	6	66.7%
69	4	2	50.0%
75	3	0	0.0%
84	92	10	10.9%
88	104	9	8.7%
89	4	0	0.0%
94	12	6	50.0%
106	16	4	25.0%

Zero-lag connectivity often involves amplitude inversion

The first 2.5 seconds of activity is shown in Figure 2.a for three typical homologous pairs with an offset-PLI > 0.1. The overlaid signals are tightly synchronized without any phase lag, but amplitude-inverted across the two hemispheres. This is equivalent to saying that these pairs of signals are synchronized in antiphase since amplitude inversion is mathematically equivalent to a 180-degree phase-shift for oscillatory signals. Further, since PLI estimates account only for phase synchronization, irrespective of amplitude differences, any in-phase and amplitude inverted (eq. in-antiphase) synchronization between two signals is discarded by PLI estimates. Therefore, zero-lag connectivity uncovered by comparing offset-PLI with standard PLI estimates should be understood as connectivity between signals shifted by any integer multiple of 180 degrees, including zero degrees.

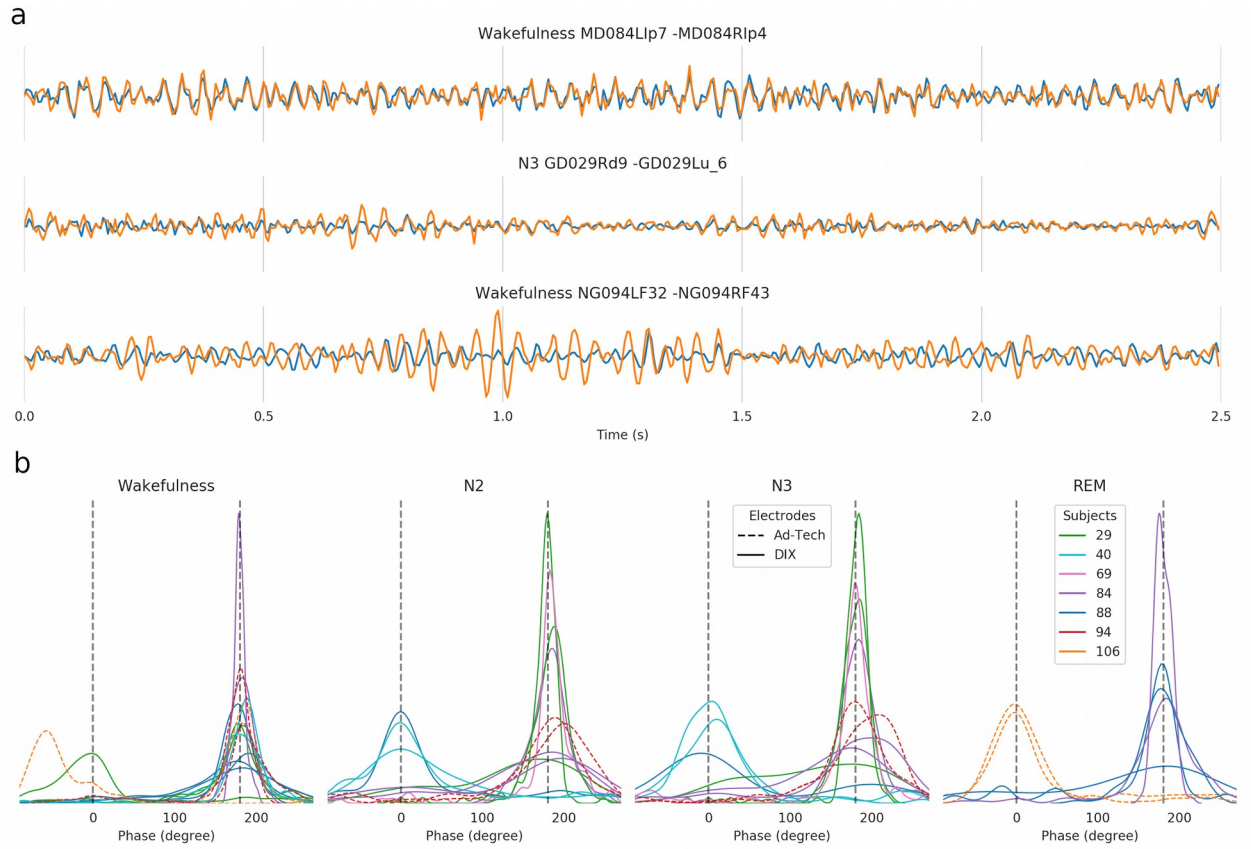

Figure 2. Amplitude inversion (eq. 180-degree phase-shifts) in zero-lag connectivity. a) First 2.5 seconds of signals from three pairs of channels from homologous regions that are highly connected with zero-lag connectivity. The title above these three plots identifies the vigilance state and the two channels being plotted. The minus sign in front of the name of the second channel indicates amplitude inversion. b) Distribution of phase differences for all homologous pairs with debiased offset-PLI > 0.1. REM: Rapid eye movement sleep; N2 and N3: Second and third stages of non-REM sleep.

To illustrate the proportion of synchrony at zero (in-phase) versus 180 degrees (in-antiphase), we plotted the distribution of the phase difference between homologous pairs with offset-PLI > 0.1 (Figure 2.b). The presence of well-defined peaks at either 0 or 180 degrees for most pairs strongly confirms our findings of zero-lag connectivity. Although peaks can be observed at both

phase-shifts, there are significantly more peaks (78%, Table 2) at 180 degrees vs. 0 degrees (p = 2.0e-05; testing against the Bernoulli distribution under the null hypothesis that the dominant phase is equally likely to be at 0 or 180 degrees). Although this test is not exact given that the 46 electrode pairs include repeated measurements on subjects and channels, the dominance of the 180-degree offset appears robust since it is observed across all vigilance states and channel types. This was also the case in most subjects (5/7) showing significant zero-lag connectivity in homologous pairs, where the percentages of 180-degree phase-shift dominance are 100%, 100%, 100%, 89%, 78%, 33%, and 25% respectively. Due to a large effect size (Cohen's d=0.83; (Cohen, 1988), the predominance of the 180-degree phase-shift is statistically significant across subjects (t=2.03; p=0.044; one-tail one-sample t-test, compared against μ=50%) even with this small sample size (N=7).

Table 2. The number of homologous pairs with significant zero-lag connectivity that are either dominated by a 0 or a 180 degrees phase-shift, per vigilance state, and electrode type.

State	Electrode	0 degree	180 degree	Percentage
N2	DIXI	3	7	70%
	Ad-Tech	0	2	100%
N3	DIXI	3	7	70%
	Ad-Tech	0	2	100%
REM	DIXI	0	5	100%
	Ad-Tech	2	0	0%
Wakefulness	DIXI	1	10	91%
	Ad-Tech	1	3	75%
Total		**10**	**36**	**78%**

Zero-lag connectivity is independent of physiological and recording conditions

We examined the extent to which zero-lag connectivity is modulated by anatomical or physiological factors, namely, brain region, vigilance state, frequency band, and recording electrode type. Among the 46 pairs that showed significant (i.e., offset-PLI > 0.1) non-lagged

196 connectivity, 37 were from the temporal lobe, eight were frontal, and one was parietal. This
197 corresponds to 16.2% (15/229), 19.5% (8/41), and 25.0% (1/4) of all homologous pairs for these
198 three regions, respectively. We also observed similar proportions of homologous pairs with non-
199 lagged connectivity across vigilance state: rapid eye movement sleep (REM) sleep (12.1%;
200 7/58), non-REM stage 2 (N2) sleep (16.9%; 12/71), non-REM stage 3 (N3) sleep (16.9%;
201 12/71), and wakefulness (20.3%; 15/74). Regarding the electrode type, all homologous pairs
202 involved the same type of electrodes in both hemispheres, and these types were either DIXI
203 electrodes (90%; 246/274) or Ad-Tech subdural strips and grids (10%; 28/274). For the subset
204 of pairs with offset-PLI > 0.1, these percentages were equal to 78% (36/46) and 22% (10/46),
205 respectively.

206 Kruskal-Wallis non-parametric one-way ANOVAs showed no significant effect of lobes or
207 vigilance states on debiased offset-PLI values in homologous pairs of electrodes. However, we
208 found a significant effect of brain regions (H=29.1; p-values=5.9e-5). This is due only to pairs
209 within the Planum Temporale. When data from this region are excluded, the region effect
210 becomes non-significant. Most pairs in the Planum Temporal have a high offset-PLI (see Figure
211 3.a). However, detailed examination (see the full table of pairs with offset-PLI > 0.1 in
212 Supplementary Table 1) shows that only two subjects are implanted bilaterally in the Planum
213 Temporale and that the higher values come from only one of these subjects. We also found a
214 significant effect of the electrode type (H=6.52; p-values=0.011; see distributions in Figure 3.b).
215 However, since both types of electrodes are well represented in the homologous pairs with
216 offset-PLI > 0.1, we can rule out the possibility that zero-lag inter-hemispheric connectivity is
217 linked to a specific type of electrode.

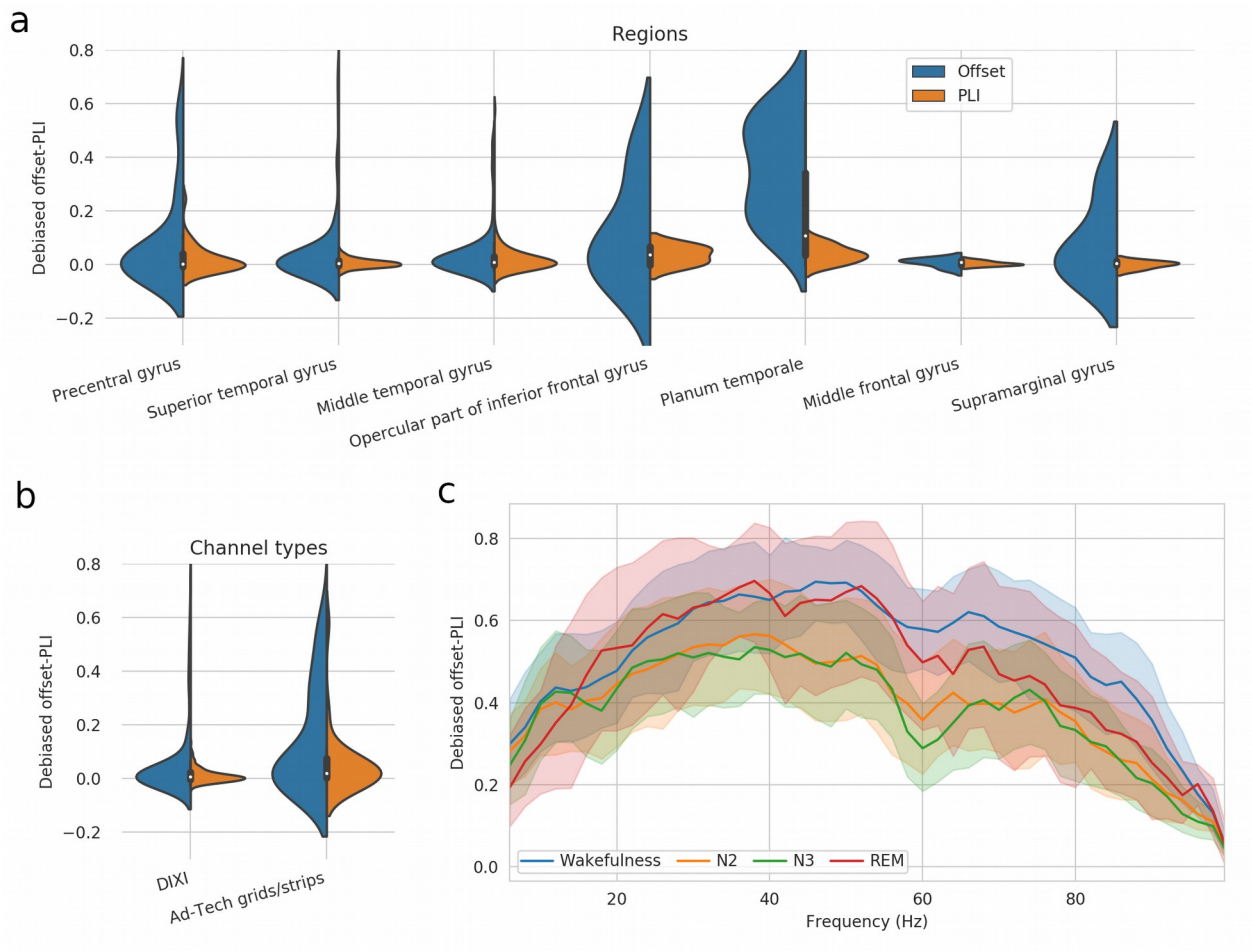

218 **Figure 3. Modulation of zero-lag connectivity by physiological or experimental factors.**
219 **a,b) Distribution of debiased PLI and offset-PLI values between homologous channels for**
220 **the different brain regions (a) and electrode types (b). c) Variation of the debiased offset-**
221 **PLI with frequency. PLI values are averaged, per vigilance state, across the homologous**
222 **pairs with overall debiased offset-PLI > 0.1.**

223 Averaged offset-PLI computed per 2 Hz frequency bands for the set of channel pairs with
224 debiased offset-PLI > 0.1 show that the zero-lag synchronization is broadband (see Figure 3.c;
225 single curves, for all 46 pairs, are also provided in Supplementary Figure 2), reflecting that large
226 populations of neurons can fire synchronously across brain regions following non-sinusoidal
227 patterns.

Discussion

Potential roles of zero-lag connectivity

Using intracranial recordings, we demonstrated ubiquitous zero-lag connectivity between homologous brain regions, which was three times more often in antiphase than in phase. It is well known that the sign of local field potentials and current source densities can alternate depending on the laminar depth within a given cortical column (Schaefer et al., 2015). Thus, it is possible that some amplitude inversions we observed are due to electrodes recording in homologous regions at different cortical depths. Nevertheless, this is unlikely to explain the relatively high and robust predominance of in-antiphase synchronization observed in our data.

A mechanism of competition/reciprocal-inhibition is likely to be involved in the observed antiphase synchronization. Previous studies using transcranial magnetic stimulation have identified a similar pattern of interhemispheric inhibition over the primary motor area (Ferbert et al., 1992; Perez and Cohen, 2009). However, to our knowledge, this is the first time phase-synchrony is reported for spontaneous interhemispheric inhibition. The observation that such inhibition happens in most cases with a synchronous phase furthers our understanding of the mechanisms involved in interhemispheric inhibition.

Regarding in-phase connectivity, synchronized activity between two brain regions, resulting from generalized depolarization at the population level, creates a common window of heightened responsiveness. Therefore, it can be hypothesized that such a window promotes information integration between these distant regions.

Zero-lag connectivity may also be involved in supporting the brain's predictive capacity. The

brain is a delayed network due to the finite conduction velocity of the electrical impulses traveling across its fibers. In such a network, the apparent paradox of zero-lag (instantaneous) connectivity can be resolved through rhythmic entrainment supported by feedback in closed-loop systems. By capturing the rhythm by which a phenomenon of interest occurs (i.e., rate coding), neuronal populations can synchronize their activity with expected external or internal cues, allowing anticipation and better response time. Therefore, such synchrony would occur bilaterally for any process requiring operations performed either in both hemispheres at the same time, or potentially in a different hemisphere at the same time, depending on the context (e.g., the laterality of a stimulus).

Implications for functional connectivity in EEG

Our findings of ubiquitous zero-lag connectivity between homologous brain regions have important implications for the measurement of functional connectivity using EEG. Traditional solutions to deal with the confounding effects of volume conduction include studying only long-range connections (e.g., considering only pairs of electrodes separated by more than 10 cm in a coherence study; (Srinivasan et al., 1998) or discarding any zero-lag connectivity (e.g., using the imaginary part of coherency or the PLI; (Nolte et al., 2004; Stam et al., 2007). In contrast, our findings clearly demonstrate the importance of zero-lag connectivity, indicating that the confounding effect of volume conduction needs to be controlled for without systematically discarding zero-lag connectivity. Instead, functional connectivity studies using EEG should adopt strategies to un-mix cortical sources such as independent component analysis (Delorme et al., 2012) or source reconstruction(Baillet et al., 2001), or use model-based approaches such as dynamic causal modeling (Kiebel et al., 2009). The latter approach may be argued to be more powerful; with adequate modeling, it could take into account other factors that are currently neglected, such as ephaptic coupling or long-distance neurochemical mediation.

Conclusion

In this study, we found ubiquitous in-phase and in-antiphase connectivity between homologous regions of the brain. This zero-lag activity was highly specific to homologous pairs of channels, which rules out any possibility that this observation is due the method confounders such as volume conductions spreading on unexpectedly long distances or correlations induced by improper use of reference electrodes since any of these factors would affect equally homologous and non-homologous regions. These results have important implications in our understanding of functional connectivity. Our findings demonstrate the preponderance of zero-lag connectivity and suggest that it probably serves fundamental mechanisms relevant to the integration and interpretation of input across distinct brain regions. In light of these results, it is clear that such synchronous activity should not be excluded from EEG connectivity analyses as an artifact.

Methods

Intracranial recording dataset

For this study, we used an open-access dataset of intracranial recordings (Frauscher et al., 2018) including 1772 channels recorded in 106 patients (54 males; mean age of 33.1 +/- 10.8 years) who were candidates for surgical treatment of drug-resistant epilepsy. Included channels were from brain regions considered “very likely to be healthy” by a consensus of two epileptologists. For each channel, an artifact-free segment of 60 seconds was recorded in an eyes-closed resting state, in rapid eye movement (REM) sleep, and in the second (N2) and third (N3) stages of non-REM sleep. Electrode positions are provided in stereotaxic space. Full description of inclusion criteria, signal preprocessing, and atlas co-registration are available in the original publication(Frauscher et al., 2018).

296 **Connectivity assessment**

297 To assess connectivity, we used the phase lag index (PLI) defined as follow (Ortiz et al., 2012;
298 Stam et al., 2007):

299 $$PLI = \left| E\left[sign\left(\mathrm{Im}\left(S_{xy} \right) \right) \right] \right| \quad (1)$$

300 with S_{xy} representing the cross-spectrum and E[x] denoting the expected value of x, which in
301 practice is estimated by averaging across epochs. This measure assesses the degree to which
302 the phases of two signals are locked in time. Importantly, it is defined such that all zero-lag
303 activity (i.e., oscillatory activity with no phase difference) is explicitly canceled-out. Note that the
304 zero-lag cancelation is not sensitive to differences in amplitude, and therefore, to amplitude
305 inversion. This implies that phase lags of 180 degrees are also discarded from estimated
306 connectivity. Consequently, we qualify as “zero-lag connectivity” any connectivity involving a
307 phase difference that is an integer multiple of 180 degrees.

308 PLI is known to be a biased estimator of functional brain connectivity (Vinck et al., 2011). This is
309 the case for most metric of functional connectivity since most of them are bound between 0.0
310 and 1.0 and will, therefore, have an average value greater than 0.0 on a random dataset. In our
311 analyses, we estimated this bias by computing PLI on a surrogate dataset obtained by randomly
312 pairing signals from different subjects. The mean value of this surrogate PLI has been removed
313 from raw PLI estimates to obtain debiased PLI values.

314 We further compare the values of two PLI estimates, the standard (debiased) PLI measure and
315 a second measure that we refer to as (debiased) offset-PLI. This second measure is computed
316 exactly like the first one, with the only difference being that one of the two signals has been
317 offset by a single time sample, allowing us to recover the zero-lag activity that was canceled-out

by the first measure. Our intracranial signals being sampled at 200 Hz, this corresponds to a 5 ms offset. The average magnitude of the connectivity at this delay can be shown not to be significantly different from other similar delays (e.g., 10 or 15 ms; see Supplementary Figure 1.a). Consequently, the portion of the connectivity that is not recovered by the offset-PLI due to the cancelation of the 5 ms-lagged connectivity is relatively negligible. This contrasts with the very significant loss of PLI connectivity when ignoring zero-lag correlations, as shown in Supplementary Figure 1.a by the very sharp and narrow drop in PLI values at zero-lag. Although PLI is not linearly decomposable by time-delays, the difference between PLI and offset-PLI values can serve as a proxy for zero-lag connectivity in electrode pairs separated by distances larger than the range of volume conduction.

Phase differences

The distribution of phase differences ($\Delta(\phi)$) between pairs of channels is determined by computing the angle from a polar representation of the cross-spectral density estimated using Welch's averaged periodogram method(Welch, 1967). The dominant peak phase discriminator (ϕ_d) indicating whether the dominant peak is at 0 or 180 degrees was evaluated using:

$$\phi_d = \log_{10}\left(\Delta(180)/\Delta(0)\right) \quad (2)$$

With this definition, a value of 1 indicates a phase distribution 10 times larger at a phase of 180 degrees than at 0 degrees, whereas a value of -1 indicates the opposite.

Software

All analyses, including PLI computation, have been performed in Python 3.7.7 using MNE 0.20.dev0 and the standard Python libraries for signal processing, statistical analysis, and data visualization (Numpy 1.18.2, Scipy 1.4.1, Pandas 1.0.1, Matplotlib 3.1.2, Seaborn 0.9.0).

Data and code availability

The intracranial EEG database is available at https://mni-open-ieegatlas.research.mcgill.ca. The code used for the analysis is accessible by sending a request to the corresponding author. Scripts will be provided as is, without restriction. It will also be deposited on the GitHub account of the corresponding author (https://github.com/christian-oreilly/intracranial_paper) upon acceptance of this manuscript.

Acknowledgments

This research is supported by the Azrieli Centre for Autism Research (ACAR). The authors would like to thank Samantha Wunderlich for proofreading this manuscript.

Author Contributions

C.O.R.: Conceptualization, data analysis, writing of the first manuscript draft, revision of the manuscript.

M.E.: Revision of the manuscript.

Declaration of Interests

Both authors report having no conflict of interests with respect to the content of this manuscript.

References

Anastassiou CA, Perin R, Markram H, Koch C. 2011. Ephaptic coupling of cortical neurons. *Nat Neurosci* **14**:217–223. doi:10.1038/nn.2727

Azevedo FAC, Carvalho LRB, Grinberg LT, Farfel JM, Ferretti REL, Leite REP, Jacob Filho W, Lent R, Herculano-Houzel S. 2009. Equal numbers of neuronal and nonneuronal cells make the human brain an isometrically scaled-up primate brain. *J Comp Neurol*

513:532–541. doi:10.1002/cne.21974

Baillet S, Mosher JC, Leahy RM. 2001. Electromagnetic brain mapping. *IEEE Signal Process Mag* **18**:14–30. doi:10.1109/79.962275

Bassett DS, Sporns O. 2017. Network neuroscience. *Nat Neurosci* **20**:353–364. doi:10.1038/nn.4502

Betzel RF, Bassett DS. 2017. Multi-scale brain networks. *NeuroImage*, Functional Architecture of the Brain **160**:73–83. doi:10.1016/j.neuroimage.2016.11.006

Bullock T. H., Mcclune MC, Achimowicz JZ, Iragui-Madoz VJ, Duckrow RB, Spencer SS. 1995. EEG coherence has structure in the millimeter domain: subdural and hippocampal recordings from epileptic patients. *Electroencephalogr Clin Neurophysiol* **95**:161–177. doi:10.1016/0013-4694(95)93347-A

Bullock T H, McClune MC, Achimowicz JZ, Iragui-Madoz VJ, Duckrow RB, Spencer SS. 1995. Temporal fluctuations in coherence of brain waves. *Proc Natl Acad Sci U S A* **92**:11568–11572.

Campo AT, Vázquez Y, Álvarez M, Zainos A, Rossi-Pool R, Deco G, Romo R. 2019. Feed-forward information and zero-lag synchronization in the sensory thalamocortical circuit are modulated during stimulus perception. *Proc Natl Acad Sci* **116**:7513–7522. doi:10.1073/pnas.1819095116

Cohen J. 1988. Statistical power analysis for the behavioral sciences, 2nd ed. ed. Hillsdale, N.J.: L. Erlbaum Associates.

Dalla Porta L, Matias FS, dos Santos AJ, Alonso A, Carelli PV, Copelli M, Mirasso CR. 2019. Exploring the Phase-Locking Mechanisms Yielding Delayed and Anticipated Synchronization in Neuronal Circuits. *Front Syst Neurosci* **13**. doi:10.3389/fnsys.2019.00041

Delorme A, Palmer J, Onton J, Oostenveld R, Makeig S. 2012. Independent EEG Sources Are

386 Dipolar. *PLOS ONE* **7**:e30135. doi:10.1371/journal.pone.0030135

387 Ferbert A, Priori A, Rothwell JC, Day BL, Colebatch JG, Marsden CD. 1992. Interhemispheric

388 inhibition of the human motor cortex. *J Physiol* **453**:525–546.

389 doi:10.1113/jphysiol.1992.sp019243

390 Frauscher B, von Ellenrieder N, Zelmann R, Doležalová I, Minotti L, Olivier A, Hall J, Hoffmann

391 D, Nguyen DK, Kahane P, Dubeau F, Gotman J. 2018. Atlas of the normal intracranial

392 electroencephalogram: neurophysiological awake activity in different cortical areas.

393 *Brain* **141**:1130–1144. doi:10.1093/brain/awy035

394 Gray CM, König P, Engel AK, Singer W. 1989. Oscillatory responses in cat visual cortex exhibit

395 inter-columnar synchronization which reflects global stimulus properties. *Nature*

396 **338**:334–337. doi:10.1038/338334a0

397 Kiebel SJ, Garrido MI, Moran R, Chen C-C, Friston KJ. 2009. Dynamic causal modeling for EEG

398 and MEG. *Hum Brain Mapp* **30**:1866–1876. doi:10.1002/hbm.20775

399 Nolte G, Bai O, Wheaton L, Mari Z, Vorbach S, Hallett M. 2004. Identifying true brain interaction

400 from EEG data using the imaginary part of coherency. *Clin Neurophysiol Off J Int Fed*

401 *Clin Neurophysiol* **115**:2292–2307. doi:10.1016/j.clinph.2004.04.029

402 Nunez PL, Srinivasan R, Westdorp AF, Wijesinghe RS, Tucker DM, Silberstein RB, Cadusch

403 PJ. 1997. EEG coherency. I: Statistics, reference electrode, volume conduction,

404 Laplacians, cortical imaging, and interpretation at multiple scales. *Electroencephalogr*

405 *Clin Neurophysiol* **103**:499–515. doi:10.1016/s0013-4694(97)00066-7

406 Ortiz E, Stingl K, Münßinger J, Braun C, Preissl H, Belardinelli P. 2012. Weighted Phase Lag

407 Index and Graph Analysis: Preliminary Investigation of Functional Connectivity during

408 Resting State in Children. *Comput Math Methods Med* **2012**. doi:10.1155/2012/186353

409 Pakkenberg B, Pelvig D, Marner L, Bundgaard MJ, Gundersen HJG, Nyengaard JR, Regeur L.

410 2003. Aging and the human neocortex. *Exp Gerontol* **38**:95–99. doi:10.1016/s0531-

5565(02)00151-1

Perez MA, Cohen LG. 2009. Interhemispheric inhibition between primary motor cortices: what have we learned? *J Physiol* **587**:725–726. doi:10.1113/jphysiol.2008.166926

Plonsey R, Heppner DB. 1967. Considerations of quasi-stationarity in electrophysiological systems. *Bull Math Biophys* **29**:657–664. doi:10.1007/BF02476917

Roelfsema PR, Engel AK, König P, Singer W. 1997. Visuomotor integration is associated with zero time-lag synchronization among cortical areas. *Nature* **385**:157–161. doi:10.1038/385157a0

Schaefer MK, Hechavarría JC, Kössl M. 2015. Quantification of mid and late evoked sinks in laminar current source density profiles of columns in the primary auditory cortex. *Front Neural Circuits* **9**:52. doi:10.3389/fncir.2015.00052

Srinivasan R, Nunez PL, Silberstein RB. 1998. Spatial filtering and neocortical dynamics: estimates of EEG coherence. *IEEE Trans Biomed Eng* **45**:814–826. doi:10.1109/10.686789

Stam CJ, Nolte G, Daffertshofer A. 2007. Phase lag index: assessment of functional connectivity from multi channel EEG and MEG with diminished bias from common sources. *Hum Brain Mapp* **28**:1178–1193. doi:10.1002/hbm.20346

Varela F, Lachaux JP, Rodriguez E, Martinerie J. 2001. The brainweb: phase synchronization and large-scale integration. *Nat Rev Neurosci* **2**:229–239. doi:10.1038/35067550

Vicente R, Gollo LL, Mirasso CR, Fischer I, Pipa G. 2008. Dynamical relaying can yield zero time lag neuronal synchrony despite long conduction delays. *Proc Natl Acad Sci U S A* **105**:17157–17162. doi:10.1073/pnas.0809353105

Vinck M, Oostenveld R, van Wingerden M, Battaglia F, Pennartz CMA. 2011. An improved index of phase-synchronization for electrophysiological data in the presence of volume-conduction, noise and sample-size bias. *NeuroImage* **55**:1548–1565.

436 doi:10.1016/j.neuroimage.2011.01.055

437 Viriyopase A, Bojak I, Zeitler M, Gielen S. 2012. When Long-Range Zero-Lag Synchronization is

438 Feasible in Cortical Networks. *Front Comput Neurosci* **6**. doi:10.3389/fncom.2012.00049

439 von Bartheld CS, Bahney J, Herculano-Houzel S. 2016. The Search for True Numbers of

440 Neurons and Glial Cells in the Human Brain: A Review of 150 Years of Cell Counting. *J*

441 *Comp Neurol* **524**:3865–3895. doi:10.1002/cne.24040

442 Welch P. 1967. The use of fast Fourier transform for the estimation of power spectra: A method

443 based on time averaging over short, modified periodograms. *IEEE Trans Audio*

444 *Electroacoustics* **15**:70–73. doi:10.1109/TAU.1967.1161901

Supplemental information

Effect of delays and epoch durations on offset-PLI

Supplementary Figure 1 shows averaged offset-PLI values for the four different vigilance states at various delays. To ensure that interpretation of these figures is not confounded by volume conduction, they have been produced using only pairs of electrodes separated by at least 35 mm and we included only pairs for which the overall debiased offset-PLI was larger than 0.1. Each time step corresponds to a 5 ms offset, given our recording sample at 200 Hz. Note that the values at step=0 correspond by definition to the standard PLI. Panels a and b show offset-PLI computed using 1 s and 5 s epochs, respectively. The same scale has been used for these two panels to highlight the effect of epoch duration on PLI computation. Not only the bias is very much impacted (not visible on this figure using debiased offset-PLI; 0.225 ± 0.014 (mean ± sd) for 5s epochs as compared to 0.102 ± 0.013 for 1s epochs), but even debiased offset-PLI takes very different values. The average values of offset-PLI vary smoothly with respect to the number of time steps, except for step=0. On the one hand, the smoothness for steps different from zero supports that most connectivity is preserved when computing PLI at an arbitrary offset close to zero. On the other hand, the sharp drop at step=0 shows the importance of zero-lag connectivity, even for channel pairs that are not expected to be sensitive to volume conduction.

Explanation of the effect of the epoch duration

We observe that the duration of the epochs has a significant difference on the rate at which the offset-PLI values decrease with increasing offsets (Supplementary Figure 1.a,b). In order to explain this relationship, we propose a model where we first penalize the connectivity by a factor ϵ equal to the ratio of the offset to the epoch duration:

$$\epsilon = \frac{|d|}{w_l f_s} \quad (1)$$

where d and w_l are the offset and the epoch length in sample numbers and f_s is the sampling frequency. This penalty accounts for reduced bleeding of the offset-PLI zero-lag cancellation within neighboring frequencies in larger epochs due to a consequent increase in spectral resolution. Panels (d) and (e) of Supplementary Figure 1 show that the pattern of canceled frequencies at different delays remains the same for these two epoch durations, but for shorter epochs, it is more blended and smoothed. Panel (f) overlay the variation of PLI by frequencies for different offsets, whereas panel (g) enlarges a small segment of these curves for the case with an offset of 20 time samples (100 ms). The sharpness of the troughs at *frequencies where PLI discards zero-lag connectivity*[1] (shown by vertical dashed lines) is clear for the 5 s epochs. By contrast, for the 1 s epochs, the zero-lag connectivity cancelation at two neighboring frequencies (e.g., 20 and 25 Hz on panel (g)) bleeds onto larger frequency intervals resulting in a very sharp and more heavily attenuated intermediate peak (e.g., at around 22.5 Hz on panel (g)). For larger epochs, the resulting higher frequency sampling is associated with smaller frequency intervals over which connectivity is canceled-out, resulting in a slower decrease of the offset-PLI as the offset increases.

While this increased attenuation due to reduced spectral resolution may account for most of the differences observed for offset-PLI across different epoch sizes, it does not account for the curved aspects of these relationships. Thus, we further scaled the ϵ penalty by a weight $w(|d|)$ proportional to the square root of the area under the $1/f^{\beta}$ aperiodic spectral component, normalized to unity and integrated from the inverse of the offset up to half the sampling

1 For a given offset Δ, the expression "*frequencies where PLI discards zero-lag connectivity*" can be understood as frequencies where the zero-lag connectivity is canceled-out both at offset=0 and offset=Δ. For example, with an offset of two time steps (a period of 10 ms), the activity that was zero-lagged at 50 Hz with offset=0 ms is again zero-lagged with offset=10 ms since the signal has been shifted by exactly half a cycle (i.e., 180 degrees) from its original phase.

frequency (i.e., the Nyquist frequency):

$$w(|d|)=\sqrt{\frac{\int_{1/d}^{f_s/2} f^{-\beta}df}{\int_{0}^{f_s/2} f^{-\beta}df}} \quad (2)$$

The square root in (2) is used to account for the fact that the $1/f^{\beta}$equation describes the aperiodic component of the *power* spectrum, which is related to the amplitude by a square relationship. β was set to 2.29, as previously reported(Frauscher et al., 2018). The *w(|d|)* factor accounts for the fact that higher frequencies are expected to be more severely affected by smaller delays because these delays constitute a larger fraction of their period. As the offset increases, we penalize the connectivity more because the offset starts to increasingly affect the lower frequencies while continuing to affect high frequencies. Finally, we scale the penalty by a single proportionality constant *a* fitted manually to a value of 12 in our analysis. The final relationship is as follow:

$$PLI(d)=1-a\epsilon\, w(|d|) \quad (3)$$

Supplementary Figure 1.c shows the variation of offset-PLI with respect to the offset as modeled with the equation (3), overlaid to the empirical curves shown in panel (a) and (b), but averaged across states and normalized to their peak. This tentative explanation captures relatively well the overall behavior displayed by the offset-PLI computed using different epoch durations, using only one free parameter (*a*).

504 **Supplementary Table 1. Homologous pairs with offset-PLI > 0.1.**

Subject	Distance	Homologous distance	State	Offset	PLI	Elec-trode	Lobe	Region
94	120	20	N2	0.212	0.113	G	Frontal	Precentral gyrus
94	126	32	N2	0.292	0.049	G	Frontal	Precentral gyrus
88	110	28	N2	0.330	0.030	D	Temporal	Middle temporal gyrus
69	118	16	N2	0.452	0.048	D	Temporal	Middle temporal gyrus
29	108	24	N2	0.171	0.036	D	Temporal	Planum temporale
29	112	24	N2	0.479	0.015	D	Temporal	Planum temporale
29	114	24	N2	0.607	0.009	D	Temporal	Planum temporale
40	118	2	N2	0.135	0.049	D	Temporal	Planum temporale
84	110	12	N2	0.410	-0.005	D	Temporal	Superior temporal gyrus
84	118	12	N2	0.152	0.055	D	Temporal	Superior temporal gyrus
40	120	20	N2	0.159	0.007	D	Temporal	Superior temporal gyrus
84	124	14	N2	0.119	0.042	D	Temporal	Superior temporal gyrus
94	120	20	N3	0.201	0.093	G	Frontal	Precentral gyrus
94	126	32	N3	0.323	0.068	G	Frontal	Precentral gyrus
88	110	28	N3	0.266	0.063	D	Temporal	Middle temporal gyrus
69	118	16	N3	0.350	0.043	D	Temporal	Middle temporal gyrus
29	108	24	N3	0.163	0.070	D	Temporal	Planum temporale
29	112	24	N3	0.508	0.043	D	Temporal	Planum temporale
29	114	24	N3	0.581	-0.001	D	Temporal	Planum temporale
40	118	2	N3	0.122	0.034	D	Temporal	Planum temporale
84	110	12	N3	0.389	0.007	D	Temporal	Superior temporal gyrus
84	118	12	N3	0.154	0.013	D	Temporal	Superior temporal gyrus
40	120	20	N3	0.154	0.006	D	Temporal	Superior temporal gyrus
84	124	14	N3	0.157	0.016	D	Temporal	Superior temporal gyrus
106	106	8	REM	0.403	0.061	G	Frontal	Opercular part of inferior frontal gyrus
106	120	8	REM	0.307	0.006	G	Parietal	Supramarginal gyrus
88	110	28	REM	0.461	0.023	D	Temporal	Middle temporal gyrus
88	114	42	REM	0.101	0.044	D	Temporal	Middle temporal gyrus
88	120	42	REM	0.379	-0.014	D	Temporal	Middle temporal gyrus
84	120	8	REM	0.286	0.005	D	Temporal	Superior temporal gyrus
84	132	10	REM	0.647	-0.002	D	Temporal	Superior temporal gyrus
106	112	18	Wake	0.507	0.051	G	Frontal	Precentral gyrus
94	120	20	Wake	0.600	0.246	G	Frontal	Precentral gyrus
94	126	32	Wake	0.538	0.026	G	Frontal	Precentral gyrus
88	106	28	Wake	0.456	0.018	D	Temporal	Middle temporal gyrus
88	110	28	Wake	0.168	0.005	D	Temporal	Middle temporal gyrus
88	110	28	Wake	0.223	0.039	D	Temporal	Middle temporal gyrus
88	114	28	Wake	0.175	-0.016	D	Temporal	Middle temporal gyrus
106	132	16	Wake	0.379	0.581	G	Temporal	Middle temporal gyrus
29	108	24	Wake	0.380	0.034	D	Temporal	Planum temporale
29	112	24	Wake	0.330	-0.006	D	Temporal	Planum temporale
29	114	24	Wake	0.273	0.083	D	Temporal	Planum temporale
40	118	2	Wake	0.524	0.094	D	Temporal	Planum temporale
84	116	10	Wake	0.548	-0.005	D	Temporal	Superior temporal gyrus
40	120	20	Wake	0.369	0.043	D	Temporal	Superior temporal gyrus
84	124	14	Wake	0.725	0.014	D	Temporal	Superior temporal gyrus

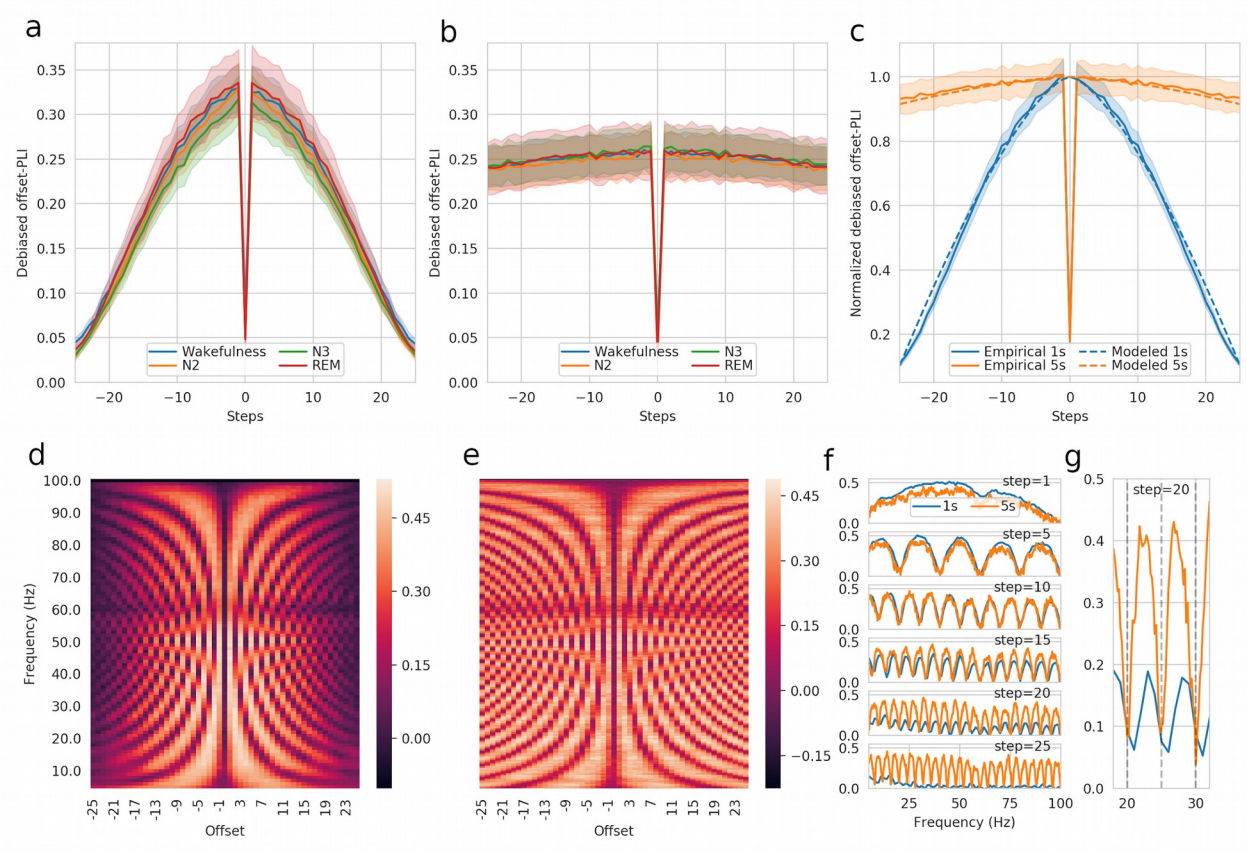

505 **Supplementary Figure 1. Impact of delays and epoch duration on PLI estimates.** a, b) Variation of
506 the offset-PLI for different offsets, for 1-s epochs (a) and 5-s epochs (b). c) Curves from panels (a) and (b)
507 averaged across states and normalized to unity at their peaks. The relationships modeled using equation
508 (3) have also been overlaid to these curves. d, e) Heat maps of offset-PLI values for a range of
509 frequencies and offsets, computed using 1 s epochs (d) and 5 s epochs (e). f) Variation of the offset-PLI
510 with respect to frequency, at discrete steps (i.e., number of time samples used as offset), overlaid for the
511 two epoch lengths. g) A zoomed-in view of the 18-32 Hz range for the offset-PLI at an offset of 20 time
512 samples (i.e., 100 ms).

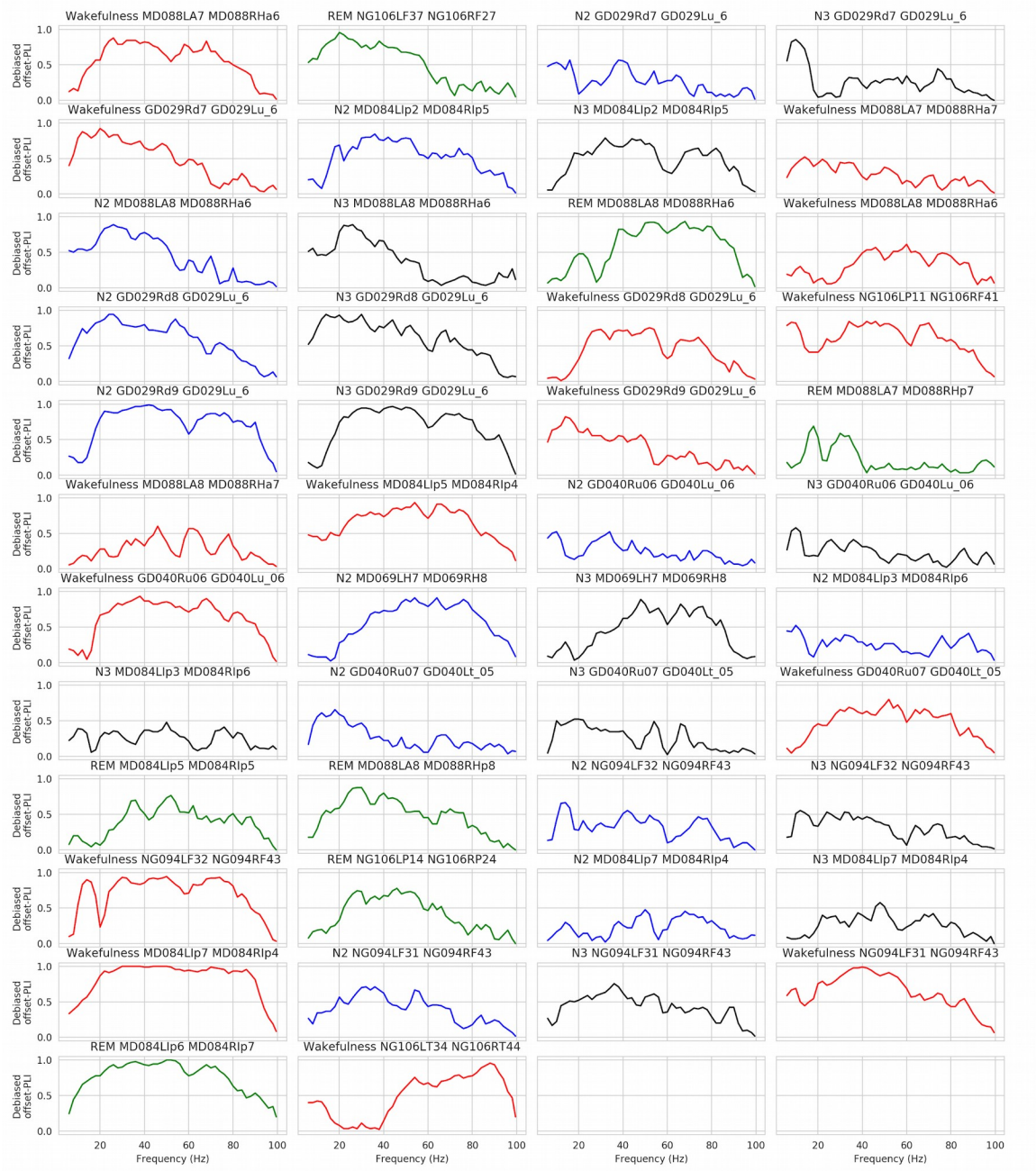

513 **Supplementary Figure 2. Variation of the debiased offset-PLI with respect to frequency for the 46**
514 **homologous pairs with a global debiased offset-PLI greater 0.1.** The title over the plots identifies the
515 vigilance state and the name of the two channels. The vigilance state is color-coded: red for wakefulness,
516 blue for N2, black for N3, and green for REM. The offset-PLI values have been computed on every
517 contiguous 2 Hz frequency band.